

Article

# A Novel, Simple and Green Way to Fabricate BiVO<sub>4</sub> with Excellent Photocatalytic Activity and Its Methylene Blue Decomposition Mechanism

Minna Guo <sup>1,2</sup>, Qianglong He <sup>1</sup>, Aiyang Wang <sup>1</sup>, Weimin Wang <sup>1,\*</sup> and Zhengyi Fu <sup>1</sup>

<sup>1</sup> State Key Laboratory of Advanced Technology for Materials Synthesis and Processing, Wuhan University of Technology, Wuhan 430070, China; guomn\_007@126.com (M.G.); qianglonghe\_whut@163.com (Q.H.); aywangwhut@163.com (A.W.); shsshshs027@163.com (Z.F.)

<sup>2</sup> College of Chemistry and Materials Science, Huaibei Normal University, 100 Dongshan Road, Anhui, Huaibei 235000, China

\* Correspondence: shswmwang@whut.edu.cn; Tel.: +86-27-87215421

Academic Editor: Helmut Cölfen

Received: 15 June 2016; Accepted: 7 July 2016; Published: 20 July 2016

**Abstract:** BiVO<sub>4</sub> photocatalysts were synthesized via a facile surfactant-free method with heat treatment. The heat treatment temperatures influenced the crystal structures and morphologies. The photocatalytic performance is associated with its crystallinity, Brunauer–Emmett–Teller (BET) specific surface area, and band gap energy. The BiVO<sub>4</sub> photocatalyst prepared by heat treatment at 700 °C showed the highest photocatalytic activity, promoting 100% degradation of methylene blue (MB) in 60 min under visible-light irradiation. Recycling experiments results indicated that the BiVO<sub>4</sub> photocatalysts have excellent photo-stability, and a possible mechanism for the photocatalytic process was proposed by examining the effects of the active species involved in MB degradation. This work could provide new insights into the fabrication of highly efficient and stable BiVO<sub>4</sub> photocatalysts for dye degradation.

**Keywords:** BiVO<sub>4</sub>; crystal structure; photocatalytic; methylene blue; decomposition mechanism

## 1. Introduction

In recent years, bismuth vanadate (BiVO<sub>4</sub>) has attracted increasing attention as a promising photocatalyst owing to its non-toxicity, high stability, and excellent photocatalytic activity in organic dye degradation and water splitting [1–8]. It has three crystalline phases [9–13], monoclinic-scheelite, tetragonal-zircon, and tetragonal-scheelite, and exhibits phase transition under certain conditions. BiVO<sub>4</sub> (s-m) is obtained when BiVO<sub>4</sub> (z-t) is heated above 350 °C–450 °C, and phase transition between BiVO<sub>4</sub> (s-m) and BiVO<sub>4</sub> (s-t) occurs reversibly at 255 °C [14].

There are numerous methods reported for the fabrication of BiVO<sub>4</sub>, including hydrothermal treatment [15–18], sonochemical method [19], sol-gel method [20–22], ionothermal treatment [23], microwave-assisted route [24,25], solution combustion synthesis [26], co-precipitation process [27], molten salt method [28], reverse microemulsion process [29], aqueous method [30–33], etc. Among all of these methods, the aqueous method provides a milder environment for the synthesis of monoclinic BiVO<sub>4</sub> and allows the reaction parameters as well as the properties of the products to be easily tuned. Akihiko et al. [30] reported an aqueous process for preparation of highly crystalline monoclinic and tetragonal BiVO<sub>4</sub> by reaction of the layered potassium vanadates KV<sub>3</sub>O<sub>8</sub> and K<sub>3</sub>V<sub>5</sub>O<sub>14</sub> with Bi(NO<sub>3</sub>)<sub>3</sub> at 20 °C for 3 d. Kohtani et al. [31] prepared BiVO<sub>4</sub> by stirring a equimolar mixture of aqueous Bi(NO<sub>3</sub>)<sub>3</sub>·5H<sub>2</sub>O and NH<sub>4</sub>VO<sub>3</sub> solutions (0.4 mol/L) containing HNO<sub>3</sub> (1.84 mol/L) with 7.5 g urea at 90 °C for 8 h. Tokunaga et al. [10] fabricated the BiVO<sub>4</sub> by an aqueous process at room temperature by

hydrolyzing a nitric acid solution of  $\text{Bi}(\text{NO}_3)_3$  and  $\text{Na}_3\text{VO}_4$  using bases ( $\text{Na}_2\text{CO}_3$  and  $\text{NaHCO}_3$ ) to adjust the pH. They found that  $\text{BiVO}_4$  (s-m) and  $\text{BiVO}_4$  (s-t) could be selectively prepared by adjusting the preparation time, and that  $\text{BiVO}_4$  (s-m) obtained using 7.0 g of  $\text{Na}_2\text{CO}_3$  showed the highest photocatalytic  $\text{O}_2$  evolution, while the activity of  $\text{BiVO}_4$  (s-t) was negligible. Yin et al. [32] synthesized a highly efficient monoclinic  $\text{BiVO}_4$  photocatalyst by an aqueous method with the assistance of cetyltrimethyl ammonium bromide (CTAB). However, base or surfactants are generally added to the reactions in order to control the crystal structure of the product, causing the production of redundant alkali wastewater containing refractory organics. Therefore, a simple surfactant-free and environmentally-friendly route is highly desirable for the preparation of photocatalysts.

In the present study, a highly efficient monoclinic  $\text{BiVO}_4$  photocatalyst for the oxidation of methylene blue (MB) under visible light irradiation was synthesized by a surfactant-free aqueous method. The effect of heat treatment temperature on the synthetic  $\text{BiVO}_4$  photocatalysts has been investigated, and their recycling stabilities were assessed. To understand the mechanism of MB decomposition over the  $\text{BiVO}_4$  system more completely, we investigated the active species involved in photocatalytic degradation.

## 2. Results

### 2.1. Phase Structures

Figure 1 shows the XRD patterns of  $\text{BiVO}_4$  samples synthesized under different conditions. The sample H0 is a heterophase comprising tetragonal zircon phase (JCPDS card No. 14-0133) and monoclinic scheelite phase (JCPDS card No. 14-0688). According to  $V_{\text{monoclinic}} = I_{\text{monoclinic}(121)} / (I_{\text{monoclinic}(121)} + I_{\text{tetragonal}(200)})$  from XRD patterns [12], the percentage of m- $\text{BiVO}_4$  is 27.47%. The samples H400, H500, H600, H700, and H800 can be well indexed to the pure monoclinic phase, from which we can see that z- $\text{BiVO}_4$  can transform into m- $\text{BiVO}_4$  when it is heated beyond 400 °C. It is worth noting that the relative intensities of the diffraction peaks  $I_{040}/I_{121}$  increase obviously with increasing heat treatment temperature, indicating a preferred (040) surface orientation for the  $\text{BiVO}_4$  crystal growth.

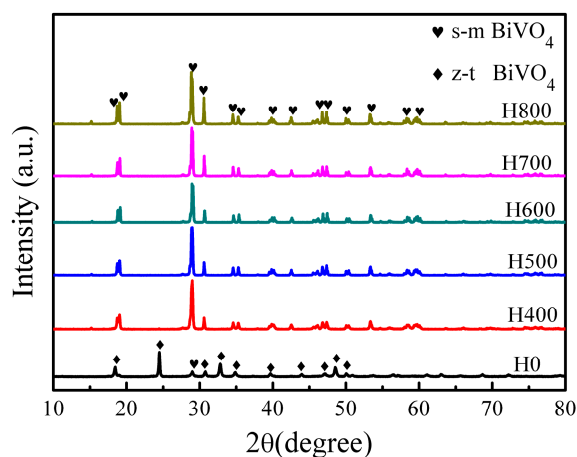


**Figure 1.** XRD patterns of the  $\text{BiVO}_4$  samples synthesized under different conditions.

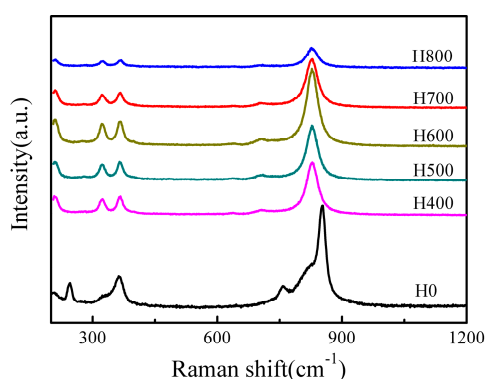
The average sizes of the crystallites with the (121) peak were calculated using the Scherrer equation ( $D = K\lambda / (\beta \cos\theta)$ ), where  $K$  is 0.89,  $\lambda$  is the X-ray wavelength (0.154 nm),  $\beta$  is the full width at half maximum, and  $\theta$  is half of the diffraction angle. The crystal sizes calculated from the (121) peaks increases as heat treatment temperature increases, varying from 55 to 69 nm, as shown in Table 1, indicating that the sample crystallinity improved as heat treatment temperature increases [33].

**Table 1.** Some selected properties of BiVO<sub>4</sub> samples.

Samples	H0	H400	H500	H600	H700	H800
Crystalline size (nm)	—	55	65	68	69	69
Bandgap (eV)	2.68	2.41	2.38	2.36	2.34	2.35
S <sub>BET</sub> (m <sup>2</sup> ·g <sup>-1</sup> )	5.4	5.4	5.6	3.2	4.9	3.2

## 2.2. Raman Spectra

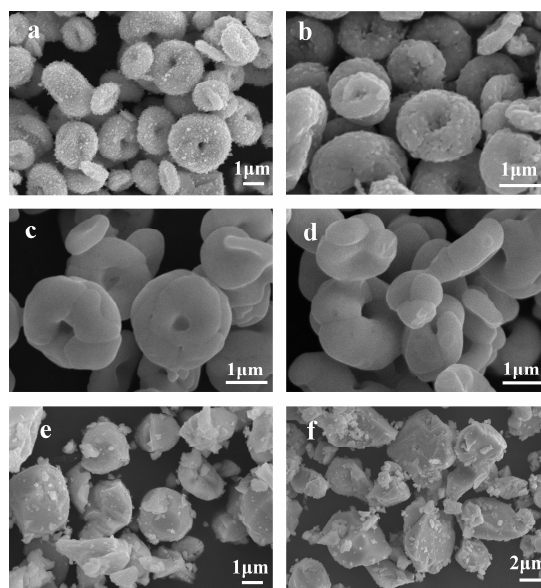
Raman spectroscopy is an appropriate technique for probing the local structure of materials because the bonding states in the coordination polyhedra of a material can be deduced directly from the Raman vibrational spectrum [34]. Thus, Raman spectroscopy was used to elucidate the local structure of the prepared BiVO<sub>4</sub> samples, and the results are presented in Figure 2. For the tetragonal zircon type BiVO<sub>4</sub> (H0), the most intense Raman band appear at 853 cm<sup>-1</sup> is ascribed to the symmetric V-O stretching mode (Ag symmetry), while the weak shoulder at about ca. 759 cm<sup>-1</sup> is assigned to the antisymmetric V-O stretching mode (Bg symmetry). The band at 364 cm<sup>-1</sup> is attributed to the O-V-O bending mode (Ag symmetry) and the band at 245 cm<sup>-1</sup> can be assigned to the Bi-O stretching mode (Eg) [35,36]. For the monoclinic scheelite type BiVO<sub>4</sub> samples (H400, H500, H600, H700 and H800), the spectra show a single band at around ca. 827 cm<sup>-1</sup> that is normally attributed to the symmetric V-O stretching mode (Ag symmetry), and the bands at around ca. 366 cm<sup>-1</sup> and 323 cm<sup>-1</sup> are ascribed to the symmetric V-O (Ag symmetry) bending mode and antisymmetric V-O (Bg symmetry) bending mode of VO<sub>4</sub> units [34,37], respectively. The external mode (rotation/translation) occurs at 210 cm<sup>-1</sup>. The V-O bond length can be calculated using the empirical expression:  $\nu$  [cm<sup>-1</sup>] = 21349 exp (-1.9176R [Å]) [38], wherein  $\nu$  is the Raman shift and R is the bond length. The calculated V-O bond length in BiVO<sub>4</sub> (s-m) (H700) is 1.696 Å, which is in well agreement with a previous report [34]. The band corresponding to the symmetric V-O (Ag) bending mode in BiVO<sub>4</sub> (s-m) appears at 366 cm<sup>-1</sup> and is larger than that at 364 cm<sup>-1</sup> in BiVO<sub>4</sub> (z-t), implying that the bond angle of O-V-O in BiVO<sub>4</sub> (s-m) is smaller than that in BiVO<sub>4</sub> (z-t) [35]. The Raman spectra reveal that the prepared BiVO<sub>4</sub> has two crystal forms, which coincides with the XRD results.

**Figure 2.** Raman spectra of the BiVO<sub>4</sub> samples synthesized under different conditions.

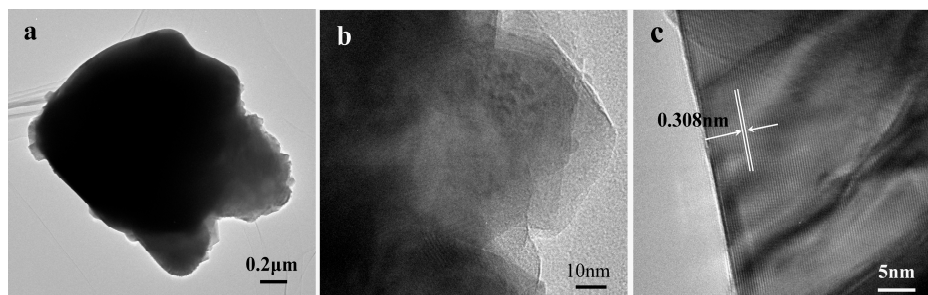
## 2.3. Morphologies of BiVO<sub>4</sub> Samples

Figure 3 shows the micrographs of the BiVO<sub>4</sub> samples observed by SEM, and indicate that heat treatment temperature has a significant influence on the samples morphologies. The sample H0 (Figure 3a) mainly presents a relatively uniform doughnut structure with a diameter of 1.5–2.5 μm formed by small crystals. After heat treatment, the morphology changes drastically. When the heat treatment temperature is 400 °C, the doughnut structure is unchanged compared with H0, but small crystals began to grow (Figure 3b). When the temperature increases further to 500 °C, the doughnut structure is still unchanged, but the crystals grow into larger grains (Figure 3c). Figure 3d shows that

when heat treatment temperature is 600 °C, the crystals grow further, and the doughnut structure tends to change to form particles. Large particles with dimensions in the range of 1–3 μm are observed following heat treatment at 700 °C (Figure 3e). It can be seen from the TEM image (Figure 4b) that the sample H700 shows a piece of materials, and the clear lattice fringes (Figure 4c) are indication of high crystallinity. The d-spacing was measured to be 0.308 nm, which agreed well with (121) plane spacing of m-BiVO<sub>4</sub>. At higher temperature (800 °C), the particles grow larger still with the largest size observed being ca. 6 μm (Figure 3f). The small irregular particles on the surfaces of particles in Figure 3e,f are derived from the grind process.



**Figure 3.** Typical SEM images of: (a) H0; (b) H400; (c) H500; (d) H600; (e) H700; and (f) H800.



**Figure 4.** (a,b) TEM images and (c) HRTEM image of sample H700.

The BET specific surface areas of the BiVO<sub>4</sub> samples synthesized under different conditions are summarized in Table 1. The specific surface area varies as heat treatment temperature changes, because the samples morphologies depended on the heat treatment temperature, and the morphology affects the specific surface area [39].

#### 2.4. UV-vis Diffuse Reflectance Spectra (UV-vis DRS)

In order to investigate the light absorption properties of the as-obtained BiVO<sub>4</sub>, UV-vis diffuse reflectance spectroscopy (UV-vis DRS) was conducted, as shown in Figure 5. All samples exhibit strong absorption in the visible-light region, and the steep shapes of the spectra suggest that the visible or UV-light adsorption can be attributed to the intrinsic transition between the valence band (VB) and the conduction band (CB), rather than to the transition from the impurity to the conduction band [40]. It is worth highlighting that the higher absorption intensity of some samples is due to

scattering phenomena linked to the sample morphology [6]. The band gap energy can be calculated by the equation  $\alpha h\nu = A (h\nu - E_g)^{1/2}$ , wherein  $\alpha$  is the absorption coefficient,  $h\nu$  is the photon energy,  $A$  is a constant ( $A = 1$ ), and  $E_g$  is the band gap energy. The band gap energy can be estimated from a plot of  $(\alpha h\nu)^2$  versus  $h\nu$ , as shown in Figure 5b, and the intercept of the tangent to the x-axis gives a good approximation the band gap energy. Accordingly, the band gap energies of samples H0, H400, H500, H600, H700 and H800 are ca. 2.68, 2.41, 2.38, 2.36, 2.34 and 2.35 eV, respectively, as shown in Table 1, which are all characteristic of the band gap for the monoclinic phase of  $\text{BiVO}_4$  (except that of H0, because H0 is a heterophase comprising tetragonal zircon phase and monoclinic scheelite phase). The difference in band gap energy demonstrates that the electronic structures of the samples change with heat treatment temperature, and the variations in the electronic structures lead to different degrees for the delocalization of photogenerated carriers, resulting in their different mobility efficiencies.

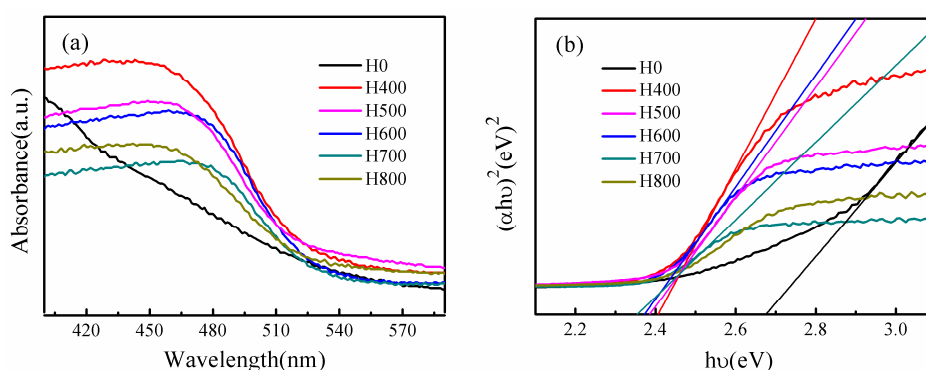


**Figure 5.** (a) UV-vis diffuse reflectance spectra, (b) Plots of  $(\alpha h\nu)^2$  versus photon energy ( $h\nu$ ) of  $\text{BiVO}_4$  synthesized under different conditions.

### 2.5. PL Analysis

Photoluminescence (PL) spectra have been widely used to disclose the migration, transfer, and recombination processes of the photogenerated electron–hole pairs in the semiconductor particles [41], PL emission mainly originates from the recombination of excited electrons and holes. Therefore, a low PL intensity implies a low electron–hole recombination rate under light irradiation [42]. Figure 6 shows the room temperature PL spectra of  $\text{BiVO}_4$  synthesized under different conditions. It is obvious that the normalized PL intensity of these samples decreases in the order of H400 > H500 > H600 > H800 > H700. The PL intensity of the H700 sample is the lowest, indicating that the retarded recombination of the holes formed in the hybrid orbitals of Bi6s and O2p (VB) and the electrons in the V3d orbitals (CB), which can lead to an enhanced photocatalytic activity.

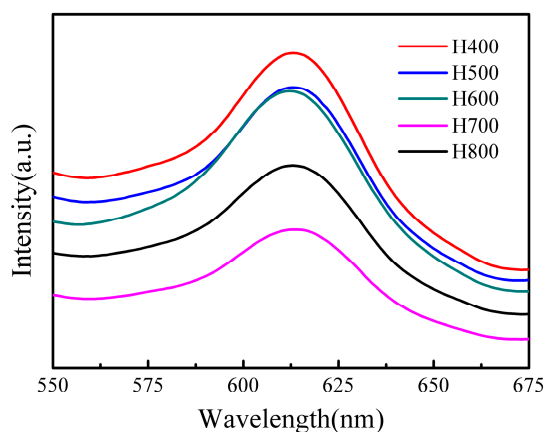


**Figure 6.** Room temperature PL spectra of  $\text{BiVO}_4$  synthesized under different conditions.

## 2.6. Photocatalytic Activity and Recycling Performance

The photocatalytic performances of the  $\text{BiVO}_4$  samples were investigated by MB degradation under visible light irradiation, the results of which are shown in Figure 7. Among all of the samples, H700 exhibits the best MB degradation efficiency, and 100% of the MB is degraded after 60 min, while 66.0%, 73.4%, 84.9%, and 97.0% of the MB is degraded after 60 min in the presence of H400, H500, H600, and H800, respectively. All samples exhibit much better photocatalytic activities than that of  $\text{TiO}_2$  photocatalyst (P25), which degrades only 9.6% of the MB after 60 min. It is worth noting that the adsorption efficiency of H0 is very high (ca. 85.6% in the dark), but its MB degradation efficiency is negligible.

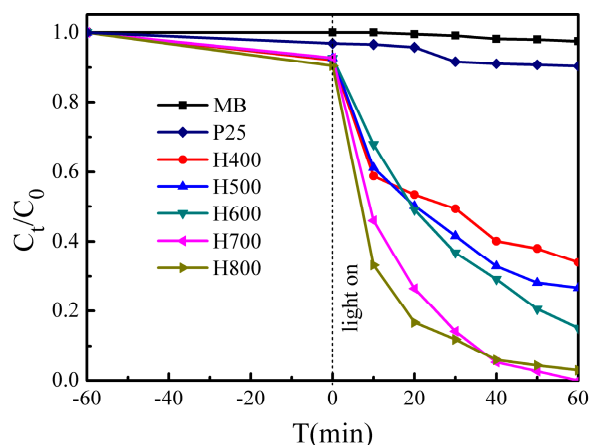


**Figure 7.** Photocatalytic activity of samples for MB degradation under visible light irradiation.

We can see that the photocatalytic performance increases with increasing heat treatment temperature until 700 °C, however, when the temperature increased further to 800 °C, the photocatalytic performance decreases. This is because the crystallinity degree increases with increasing the heat treatment temperature, and a highly crystalline structure suppresses the recombination of photogenerated electron–hole pairs [39]; but the surface area of H800 ( $3.2 \text{ m}^2 \cdot \text{g}^{-1}$ ) is smaller than that of H700 ( $4.9 \text{ m}^2 \cdot \text{g}^{-1}$ ), and the high surface area supplies more active sites for the degradation of MB, and promotes the electron–hole pairs separation effectively [43]. Furthermore, H700 exhibits the lowest band gap energy, and the lower the band gap energy, the higher the photocatalytic performance [44].

These results reflect the discrepancy in the photocatalytic performance of the samples. Therefore, these observations indicate that the crystallinity, BET specific surface area, and band gap energy should be considered as having a combined effect on the photocatalytic performance.

The stability and reusability of a catalyst is important for its practical applications, and thus the photo-stability of the synthesized H700 photocatalyst was evaluated in repeated photocatalytic experiments under the same reaction conditions. Figure 8 shows the MB degradation efficiency during each 60 min cycle. The results show that the photocatalyst exhibits no loss of activity over five cycling runs. The H700 photocatalyst used in the cycling tests was characterized using SEM and XRD before and after the cycling experiments. The corresponding XRD (Figure 9a) and SEM micrograph (Figure 9b) show that the catalysts exhibit no observable changes in crystal structure and morphology. These results suggest that the as-obtained  $\text{BiVO}_4$  sample does not suffer from photo corrosion, and has excellent stability and reusability for the degradation process.

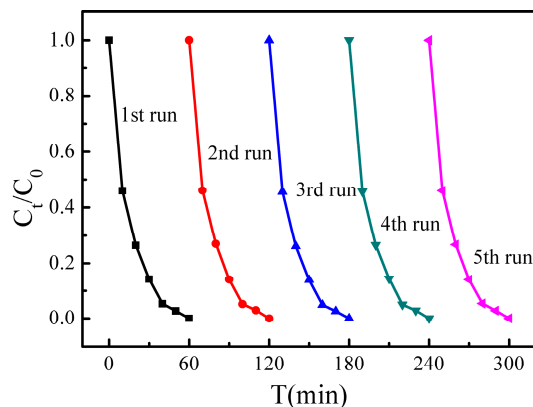


**Figure 8.** Cyclic photocatalytic degradation experiments of MB by H700 photocatalyst.

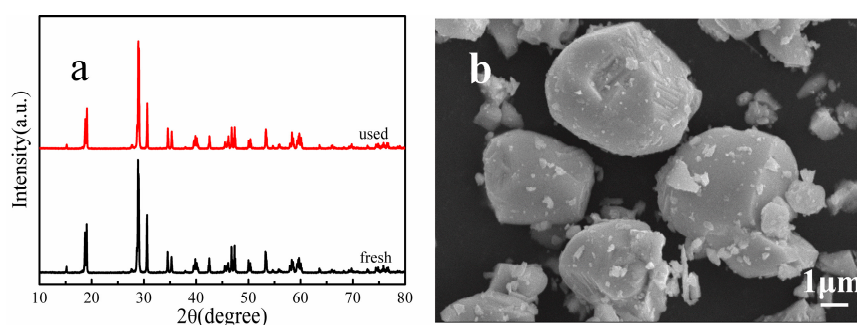


**Figure 9.** (a) XRD patterns and (b) SEM micrograph of sample H700 before and after the photo-stability tests.

### 2.7. Trapping Experiments

We performed reactive species trapping experiments to detect the main oxidative species ( $h^+$ ,  $\bullet O_2^-$  and  $\bullet OH$ ) in the photocatalytic reaction to further clarify the photocatalytic mechanism for  $BiVO_4$ . In this study, tert-butanol ( $t$ -BuOH, a  $\bullet OH$  radical scavenger), p-benzoquinone (BZQ, an  $\bullet O_2^-$  radical scavenger), and disodium ethylene diamine tetra acetate ( $Na_2$ -EDTA, a hole scavenger) were used [45,46]. As shown in Figure 10, when  $t$ -BuOH is added, the photocatalytic activity does not change, implying that  $\bullet OH$  radicals are not the main oxidative species in this process. However, the introduction of  $Na_2$ -EDTA reduces the photocatalytic activity from 100% to 52.3% in 60 min, and the presence of BZQ also causes deactivation of the H700 photocatalyst. These results suggest that  $h^+$  and  $\bullet O_2^-$  radicals play a dominant role in the  $BiVO_4$  system, and  $\bullet OH$  radicals are not involved.

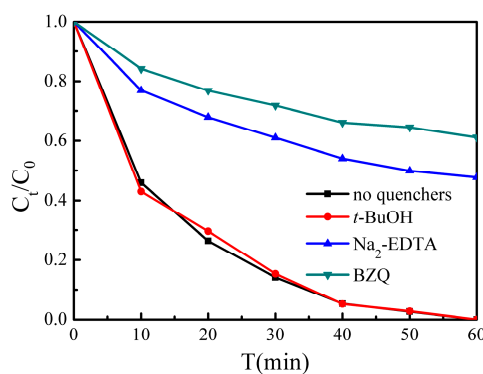


**Figure 10.** Reactive species trapping experiments of MB over H700 photocatalyst under visible light irradiation.

Based on the reactive species trapping experiment results, a proposed mechanism for MB photocatalytic degradation by  $\text{BiVO}_4$  photocatalysts is shown in Figure 11. Under visible light irradiation, photoinduced holes ( $\text{h}^+$ ) are generated in the VB by the photoinduced transfer of electrons ( $\text{e}^-$ ) from the VB to the CB. The  $\text{e}^-$  are scavenged by oxygen to form  $\bullet\text{O}_2^-$  radicals, which can degrade MB effectively. Meanwhile, the  $\text{h}^+$  in the VB can oxidize MB to its degradation products directly.

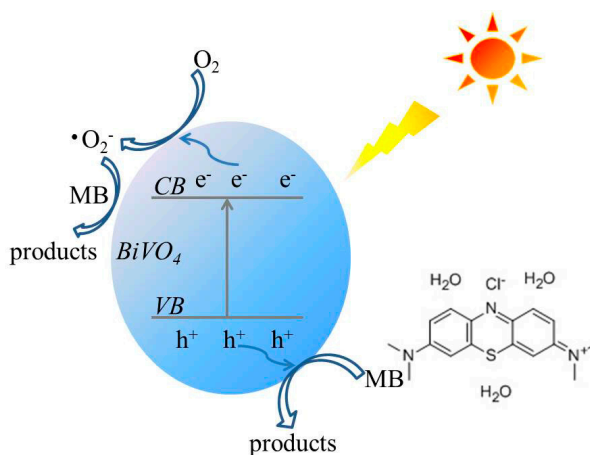


**Figure 11.** The schematic diagram of charge separation and photocatalytic process of the  $\text{BiVO}_4$  photocatalysts under visible light irradiation.

### 3. Materials and Methods

#### 3.1. Catalyst Preparation

All reagents and solvents were purchased from commercial sources and used without further purification.  $\text{Bi}(\text{NO}_3)_3 \cdot 5\text{H}_2\text{O}$ ,  $\text{NH}_4\text{VO}_3$ , and acetic acid (36%) were purchased from Sinopharm Chemical Reagent, China.

In a typical synthesis procedure, 5 mmol  $\text{Bi}(\text{NO}_3)_3 \cdot 5\text{H}_2\text{O}$  was dissolved in 25 mL acetic acid (36%) under magnetic stirring for 30 min at room temperature to form solution A; 5 mmol  $\text{NH}_4\text{VO}_3$  was dissolved in 25 mL deionized water under magnetic stirring for 30 min at 70 °C to form solution B. Solution B was added dropwise into solution A under stirring. Subsequently, the mixture was put into a water bath and heated at 90 °C for 24 h. After completion of the reaction, the precipitates were filtered, repeatedly washed with deionized water and absolute ethanol, and dried overnight at 60 °C. Then, the obtained sample was heated to 400, 500, 600, 700 and 800 °C for 2 h with a ramp rate of 5 °C·min<sup>-1</sup> via muffle furnace, which can be denoted as H400, H500, H600, H700, and H800, respectively, and the sample without heat treatment is named as H0.

#### 3.2. Characterization

The crystal structures of the photocatalysts were determined by X-ray diffraction (XRD, Rigaku Ultima III, Tokyo, Japan). The visible light Raman spectra were recorded using a RENISHAW Raman microscope (Raman, INVIA, London, UK) using 633 nm lasers. The morphologies were investigated by scanning electron microscopy (SEM, Hitachi S-3400N II, Tokyo, Japan) and transmission electron microscopy (TEM, JEM2100F, Japan). The Brunauer–Emmett–Teller (BET) specific surface areas ( $S_{\text{BET}}$ ) were obtained from  $\text{N}_2$  adsorption–desorption isotherms determined at liquid  $\text{N}_2$  temperature on an automatic analyzer (ASAP 2020M, Atlanta, GA, USA). Ultraviolet-visible diffuse reflectance spectra (UV-vis DRS) was performed using a UV-vis spectrometer (Shimadzu UV-2550, Tokyo, Japan) with  $\text{BaSO}_4$  as a reference. The photoluminescence (PL) spectra of photocatalysts were recorded using Fluorescence Spectrophotometer (FP-6500, Tokyo, Japan) equipped with a Xe lamp, at an excitation wavelength of 355 nm.

### 3.3. Photocatalytic Activity

The photocatalytic activities of the samples were evaluated based on MB decolorization using a 350 W Xe-illuminator as the light source. A 420 nm cut-off filter was placed between the Xe-illuminator and the reactor. The powder (0.1 g) was added to 100 mL of MB solution with a concentration of 10 mg/L. The solution was stirred in the dark for 60 min to achieve adsorption–desorption equilibrium between the MB molecules and catalyst particles prior to light irradiation. At various irradiation time intervals, 3 mL suspensions were collected, and centrifuged to remove the photocatalyst particles. The concentrations of the remnant MB were then monitored using a UV-vis spectrometer (Shimadzu UV-2550, Toyko, Japan) at a wavelength of 665 nm.

Cycling experiments were conducted to evaluate the stability of the BiVO<sub>4</sub> photocatalyst. After each cycle, the samples were washed with deionized water and absolute ethanol, and then added to fresh MB solution after dried, followed by another cycle.

To explore the decomposition mechanism, reactive species trapping experiments were conducted, in which tert-butanol (*t*-BuOH, a •OH radical scavenger), *p*-benzoquinone (BZQ, an •O<sub>2</sub><sup>−</sup> radical scavenger), and disodium ethylene diamine tetra acetate (Na<sub>2</sub>-EDTA, a hole scavenger) were added, respectively, into the MB solution prior to addition of the photocatalyst.

## 4. Conclusions

In summary, BiVO<sub>4</sub> samples have been successfully synthesized by a surfactant free aqueous method with heat treatment, and the temperature of the heat treatment strongly affected the crystal phases, morphology, crystallinity, BET specific surface area, and band gap energy of the samples. The photocatalytic activities of the synthetic BiVO<sub>4</sub> samples were influenced by the combined effect of their crystallinity, BET specific surface area, and band gap energy. When the heat treatment temperature was 700 °C, the obtained sample showed the best photocatalytic activity. In addition, the BiVO<sub>4</sub> photocatalysts exhibited excellent stability and reusability, and photogenerated holes (h<sup>+</sup>) and •O<sub>2</sub><sup>−</sup> radicals are the predominant oxidative species in the BiVO<sub>4</sub> system.

**Acknowledgments:** The authors acknowledge the financial support from the National Science Foundation of China (U12301013) and the National Science Foundation of China (51521001).

**Author Contributions:** Weimin Wang and Minna Guo conceived and designed the experiments; Minna Guo performed the experiments; Minna Guo and Qianglong He analyzed the data; Aiyang Wang and Zhengyi Fu contributed reagents/materials/analysis tools; and Minna Guo wrote the paper.

**Conflicts of Interest:** The authors declare no conflict of interest.

## References

1. Chang, X.X.; Wang, T.; Zhang, P.; Zhang, J.J.; Li, A.; Gong, J.L. Enhanced surface reaction kinetics and charge separation of p-n heterojunction Co<sub>3</sub>O<sub>4</sub>/BiVO<sub>4</sub> photoanodes. *J. Am. Chem. Soc.* **2015**, *137*, 8356–8359. [[CrossRef](#)] [[PubMed](#)]
2. Ji, K.M.; Dai, H.X.; Deng, J.G.; Zang, H.J.; Arandiyani, H.; Xie, S.H.; Yang, H.G. 3DOM BiVO<sub>4</sub> supported silver bromide and noble metals: High-performance photocatalysts for the visible-light-driven degradation of 4-chlorophenol. *Appl. Catal. B Environ.* **2015**, *168–169*, 274–282. [[CrossRef](#)]
3. Li, H.Y.; Sun, Y.J.; Cai, B.; Gan, S.Y.; Han, D.X.; Niu, L.; Wu, T.S. Hierarchically Z-scheme photocatalyst of Ag@AgCl decorated on BiVO<sub>4</sub> (040) with enhancing photoelectrochemical and photocatalytic performance. *Appl. Catal. B Environ.* **2015**, *170–171*, 206–214. [[CrossRef](#)]
4. Gu, S.N.; Li, W.J.; Wang, F.Z.; Wang, S.Y.; Zhou, H.L.; Li, H.D. Synthesis of buckhorn-like BiVO<sub>4</sub> with a shell of CeOx nanodots: Effect of heterojunction structure on the enhancement of photocatalytic activity. *Appl. Catal. B Environ.* **2015**, *170–171*, 186–194. [[CrossRef](#)]
5. Hernandez, S.; Barbero, G.; Saracco, G.; Alexe-Ionescu, A.L. Considerations on oxygen bubble formation and evolution on BiVO<sub>4</sub> porous anodes used in water splitting photoelectrochemical cells. *J. Phys. Chem. C* **2015**, *119*, 9916–9925. [[CrossRef](#)]

6. Thalluri, S.M.; Hernández, S.; Bensaid, S.; Saracco, G.; Russo, N. Green-synthesized W- and Mo-doped BiVO<sub>4</sub> oriented along the {040} facet with enhanced activity for the sun-driven water oxidation. *Appl. Catal. B Environ.* **2016**, *180*, 630–636. [[CrossRef](#)]
7. Wu, Q.; Chen, P.F.; Zhao, L.; Wu, J.; Qi, X.M.; Yao, W.F. Photocatalytic behavior of BiVO<sub>4</sub> immobilized on silica fiber via a combined alcohol-thermal and carbon nanofibers template route. *Catal. Commun.* **2014**, *49*, 29–33. [[CrossRef](#)]
8. Guo, M.N.; Wang, Y.; He, Q.L.; Wang, W.J.; Wang, W.M.; Fu, Z.Y.; Wang, H. Enhanced photocatalytic activity of S-doped BiVO<sub>4</sub> photocatalysts. *RSC Adv.* **2015**, *5*, 58633–58639. [[CrossRef](#)]
9. Fan, H.M.; Jiang, T.F.; Li, H.Y.; Wang, D.J.; Wang, L.L.; Zhai, J.L.; He, D.Q.; Wang, P.; Xie, T.F. Effect of BiVO<sub>4</sub> crystalline phases on the photoinduced carriers behavior and photocatalytic activity. *J. Phys. Chem. C* **2012**, *116*, 2425–2430. [[CrossRef](#)]
10. Tokunaga, S.; Kato, H.; Kudo, A. Selective preparation of monoclinic and tetragonal BiVO<sub>4</sub> with scheelite structure and their photocatalytic properties. *Chem. Mater.* **2001**, *13*, 4624–4628. [[CrossRef](#)]
11. Shen, Y.; Huang, M.L.; Huang, Y.; Lin, J.M.; Wu, J.H. The synthesis of bismuth vanadate powders and their photocatalytic properties under visible light irradiation. *J. Alloys Compd.* **2010**, *496*, 287–292. [[CrossRef](#)]
12. Ke, D.N.; Peng, T.Y.; Ma, L.; Cai, P.; Dai, K. Effects of hydrothermal temperature on the microstructures of BiVO<sub>4</sub> and its Photocatalytic O<sub>2</sub> evolution activity under visible light. *Inorg. Chem.* **2009**, *48*, 4685–4691. [[CrossRef](#)] [[PubMed](#)]
13. Xu, J.; Wang, W.Z.; Wang, J.; Liang, Y.J. Controlled fabrication and enhanced photocatalytic performance of BiVO<sub>4</sub>@CeO<sub>2</sub> hollow microspheres for the visible-light-driven degradation of rhodamine B. *Appl. Surf. Sci.* **2015**, *349*, 529–537. [[CrossRef](#)]
14. Bierlein, J.D.; Sleight, A.W. Ferroelasticity in BiVO<sub>4</sub>. *Solid State Commun.* **1975**, *16*, 69–70. [[CrossRef](#)]
15. Sun, J.X.; Chen, G.; Wu, J.Z.; Dong, H.J.; Xiong, G.H. Bismuth vanadate hollow spheres: Bubble template synthesis and enhanced photocatalytic properties for photodegradation. *Appl. Catal. B Environ.* **2013**, *132–133*, 304–314. [[CrossRef](#)]
16. Dong, S.Y.; Feng, J.L.; Li, Y.K.; Hu, L.M.; Liu, M.L.; Wang, Y.F.; Pi, Y.Q.; Sun, J.Y.; Sun, J.H. Shape-controlled synthesis of BiVO<sub>4</sub> hierarchical structures with unique natural-sunlight-driven photocatalytic activity. *Appl. Catal. B Environ.* **2014**, *152–153*, 413–424. [[CrossRef](#)]
17. Wang, W.Z.; Huang, X.W.; Wu, S.; Zhou, Y.X.; Wang, L.J.; Shi, H.L.; Liang, Y.J.; Zou, B. Preparation of p-n junction Cu<sub>2</sub>O/BiVO<sub>4</sub> heterogeneous nanostructures with enhanced visible-light photocatalytic activity. *Appl. Catal. B Environ.* **2013**, *134–135*, 293–301. [[CrossRef](#)]
18. Obregón, S.; Colón, G. Excellent photocatalytic activity of Yb<sup>3+</sup>, Er<sup>3+</sup> co-doped BiVO<sub>4</sub> photocatalyst. *Appl. Catal. B Environ.* **2014**, *152–153*, 328–334. [[CrossRef](#)]
19. Zhou, L.; Wang, W.Z.; Liu, S.W.; Zhang, L.S.; Xu, H.L.; Zhu, W. A sonochemical route to visible-light-driven high-activity BiVO<sub>4</sub> photocatalyst. *J. Mol. Catal. A Chem.* **2006**, *252*, 120–124. [[CrossRef](#)]
20. Shan, L.W.; Wang, G.L.; Suriyaprakash, J.; Li, D.; Liu, L.Z.; Dong, L.M. Solar light driven pure water splitting of B-doped BiVO<sub>4</sub> synthesized via a sol-gel method. *J. Alloys Compd.* **2015**, *636*, 131–137. [[CrossRef](#)]
21. Ou, M.; Zhong, Q.; Zhang, S.L. Synthesis and characterization of g-C<sub>3</sub>N<sub>4</sub>/BiVO<sub>4</sub> composite photocatalysts with improved visible-light-driven photocatalytic performance. *J. Sol-Gel Sci. Technol.* **2014**, *72*, 443–454. [[CrossRef](#)]
22. Shan, L.W.; Liu, H.G.; Wang, G.L. Preparation of tungsten-doped BiVO<sub>4</sub> and enhanced photocatalytic activity. *J. Nanopart. Res.* **2015**, *17*, 181. [[CrossRef](#)]
23. Liu, W.; Yu, Y.Q.; Cao, L.X.; Su, G.; Liu, X.Y.; Zhang, L.; Wang, Y.G. Synthesis of monoclinic structured BiVO<sub>4</sub> spindly microtubes in deep eutectic solvent and their application for dye degradation. *J. Hazard. Mater.* **2010**, *181*, 1102–1108. [[CrossRef](#)] [[PubMed](#)]
24. Yan, Y.; Sun, S.F.; Song, Y.; Yan, X.; Guan, W.S.; Liu, X.L.; Shi, W.D. Microwave-assisted in situ synthesis of reduced graphene oxide-BiVO<sub>4</sub> composite photocatalysts and their enhanced photocatalytic performance for the degradation of ciprofloxacin. *J. Hazard. Mater.* **2013**, *250–251*, 106–114. [[CrossRef](#)] [[PubMed](#)]
25. Obregón, S.; Colón, G. Heterostructured Er<sup>3+</sup> doped BiVO<sub>4</sub> with exceptional photocatalytic performance by cooperative electronic and luminescence sensitization mechanism. *Appl. Catal. B Environ.* **2014**, *158–159*, 242–249. [[CrossRef](#)]
26. Jiang, H.Q.; Endo, H.; Natori, H.; Nagai, M.; Kobayashi, K. Fabrication and photoactivities of spherical-shaped BiVO<sub>4</sub> photocatalysts through solution combustion synthesis method. *J. Eur. Ceram. Soc.* **2008**, *28*, 2955–2962. [[CrossRef](#)]

27. Yu, J.Q.; Zhang, Y.; Kudo, A. Synthesis and photocatalytic performances of BiVO<sub>4</sub> by ammonia co-precipitation process. *J. Solid State Chem.* **2009**, *182*, 223–228. [[CrossRef](#)]
28. Liu, Y.; Ma, J.F.; Liu, Z.S.; Dai, C.H.; Song, Z.W.; Sun, Y.; Fang, J.R.; Zhao, J.G. Low-temperature synthesis of BiVO<sub>4</sub> crystallites in molten salt medium and their UV-vis absorption. *Ceram. Int.* **2010**, *36*, 2073–2077. [[CrossRef](#)]
29. Chung, C.Y.; Lu, C.H. Reverse-microemulsion preparation of visible-light-driven nano-sized BiVO<sub>4</sub>. *J. Alloys Comp.* **2010**, *502*, L1–L5. [[CrossRef](#)]
30. Akihiko, K.; Keiko, O.; Hideki, K. A novel aqueous process for preparation of crystal form-controlled and highly crystalline BiVO<sub>4</sub> powder from layered vanadates at room temperature and its photocatalytic and photophysical properties. *J. Am. Chem. Soc.* **1999**, *121*, 11459–11467.
31. Kohtani, S.; Makino, S.; Kudo, A.; Tokumura, K.; Ishigaki, Y.; Matsunaga, T.; Nikaido, O.; Hayakawa, K.; Nakagaki, R. Photocatalytic degradation of 4-n-Nonylphenol under irradiation from solar simulator: Comparison between BiVO<sub>4</sub> and TiO<sub>2</sub> photocatalysts. *Chem. Lett.* **2002**, *31*, 600–601. [[CrossRef](#)]
32. Yin, W.Z.; Wang, W.Z.; Zhou, L.; Sun, S.M.; Zhang, L. CTAB-assisted synthesis of monoclinic BiVO<sub>4</sub> photocatalyst and its highly efficient degradation of organic dye under visible-light irradiation. *J. Hazard. Mater.* **2010**, *173*, 194–199. [[CrossRef](#)] [[PubMed](#)]
33. Kho, Y.K.; Teoh, W.Y.; Iwase, A.; Madler, L.; Kudo, A.; Amal, R. Flame preparation of visible-light-responsive BiVO<sub>4</sub> oxygen evolution photocatalysts with subsequent activation via aqueous route. *ACS Appl. Mater. Interfaces* **2011**, *3*, 1997–2004. [[CrossRef](#)] [[PubMed](#)]
34. Yu, J.Q.; Kudo, A. Effects of structural variation on the photocatalytic performance of hydrothermally synthesized BiVO<sub>4</sub>. *Adv. Funct. Mater.* **2006**, *16*, 2163–2169. [[CrossRef](#)]
35. Li, G.Q.; Bai, Y.; Zhang, W.F. Difference in valence band top of BiVO<sub>4</sub> with different crystal structure. *Mater. Chem. Phys.* **2012**, *136*, 930–934. [[CrossRef](#)]
36. Yi, J.; Zhao, Z.Y.; Wang, Y.A.; Zhou, D.C.; Ma, C.S.; Cao, Y.C.; Qiu, J.B. Monophasic zircon-type tetragonal Eu<sub>1-x</sub>Bi<sub>x</sub>VO<sub>4</sub> solid-solution: Synthesis, characterization, and optical properties. *Mater. Res. Bull.* **2014**, *57*, 306–310. [[CrossRef](#)]
37. Zhou, B.; Zhao, X.; Liu, H.J.; Qu, J.H.; Huang, C.P. Synthesis of visible-light sensitive M-BiVO<sub>4</sub> (M=Ag, Co, and Ni) for the photocatalytic degradation of organic pollutants. *Sep. Purif. Tech.* **2011**, *77*, 275–282. [[CrossRef](#)]
38. Hardcastle, F.D.; Wachs, I.E. Molecular structure of molybdenum oxide in bismuth molybdates by raman spectroscopy. *J. Phys. Chem.* **1991**, *95*, 5031.
39. Zhou, Y.; Vuille, K.; Heel, A.; Probst, B.; Kontic, R.; Patzke, G.R. An inorganic hydrothermal route to photocatalytically active bismuth vanadate. *Appl. Catal. A Gen.* **2010**, *375*, 140–148. [[CrossRef](#)]
40. Kudo, A.; Tsuji, I.; Kato, H. AgInZn<sub>7</sub>S<sub>9</sub> solid solution photocatalyst for H<sub>2</sub> evolution from aqueous solutions under visible light irradiation. *Chem. Commun.* **2002**, 1958–1959. [[CrossRef](#)]
41. Chang, W.S.; Li, Y.C.M.; Chung, T.W.; Lin, Y.S.; Huang, C.M. Toluene decomposition using silver vanadate/SBA-15 photocatalysts: DRIFTS study of surface chemistry and recyclability. *Appl. Catal. A Gen.* **2011**, *407*, 224–230. [[CrossRef](#)]
42. Pan, G.T.; Huang, C.M.; Peng, P.Y.; Yang, T.C.K. Nano-scaled silver vanadates loaded on mesoporous silica: Characterization and photocatalytic activity. *Catal. Today* **2011**, *164*, 377–383. [[CrossRef](#)]
43. Li, G.S.; Zhang, D.Q.; Yu, J.C. Ordered mesoporous BiVO<sub>4</sub> through nanocasting: A superior visible light-driven photocatalyst. *Chem. Mater.* **2008**, *20*, 3983–3992. [[CrossRef](#)]
44. Yao, M.M.; Liu, M.X.; Gan, L.H.; Zhao, F.Q.; Fan, X.Z.; Zhu, D.Z.; Xu, Z.J.; Hao, Z.X.; Chen, L.W. Monoclinic mesoporous BiVO<sub>4</sub>: Synthesis and visible-light-driven photocatalytic property. *Colloids Surf. A Physicochem. Eng. Aspects* **2013**, *433*, 132–138. [[CrossRef](#)]
45. Lei, L.W.; Jin, H.H.; Zhang, Q.; Xu, J.; Gao, D.; Fu, Z.Y. A novel enhanced visible-light-driven photocatalyst via hybridization of nanosized BiOCl and graphitic C<sub>3</sub>N<sub>4</sub>. *Dalton Trans.* **2015**, *44*, 795–803. [[CrossRef](#)] [[PubMed](#)]
46. Yu, H.J.; Yu, Y.; Liu, J.H.; Ma, P.Y.; Wang, Y.C.; Zhang, F.; Fu, Z.Y. Space-confined growth of Ag<sub>3</sub>PO<sub>4</sub> nanoparticles within WS<sub>2</sub> sheets: Ag<sub>3</sub>PO<sub>4</sub>/WS<sub>2</sub> composites as visible-light-driven photocatalysts for decomposing dyes. *J. Mater. Chem. A* **2015**, *3*, 19439–19444.

